Space-time energy spectra in turbulent shear flows

Ting Wu[1,2] and Guowei He[1,2,*]

[1]*The State Key Laboratory of Nonlinear Mechanics, Institute of Mechanics,*
Chinese Academy of Sciences, Beijing 100190, China
[2]*School of Engineering Sciences, University of Chinese Academy of Sciences, Beijing 100049, China*

This article presents a review and perspectives on the models for space-time energy spectra in turbulent shear flows. The Taylor, Kraichnan-Tennekes, and elliptic approximation (EA) models are re-examined in terms of the picture of turbulent passage, which is proposed by Taylor's frozen-flow hypothesis and the Kraichnan-Tennekes random sweeping hypothesis; the stochastic dynamic models for reproduction of space-time energy spectra, such as dynamic autoregression model, are discussed; and the statistical models for reconstruction of space-time energy spectra from incomplete data sets in experimental measurements are revisited. We present three distinct approaches of successive approximation for developing the models of space-time energy spectra and use the conditional moments of energy distribution to characterize space-time energy spectra, such as propagation velocities and spectral bandwidths.

I. INTRODUCTION

In this article, we present a review and perspectives on space-time energy spectra in turbulent flows. A space-time energy spectrum or frequency wave-number energy spectrum describes the energy distribution of velocity fluctuations over a broad range of spatial and temporal length scales [1]. It not only characterizes dynamic coupling between spatial and temporal scales [2,3] and coherent structures in turbulent flows [4] but also plays a key role in flow-generated noise and flow-structure interaction [5–8], especially at large Reynolds numbers. Recently, physics-based and data-driven models have been developed for reproducing and predicting space-time energy spectra. This article is not meant to be an exhaustive review but rather is focused on the physical understanding and stochastic models of space-time energy spectra from the authors' view.

In his seminal paper on the spectrum of turbulence, Taylor [9] proposed that small-scale eddies in turbulent flows move downstream at a constant speed with little distortion. This is the famous Taylor's frozen-flow hypothesis or simply Taylor's model. It is not only used to convert the temporal spectra to spatial spectra in experimental measurements but also serves as a basic picture of turbulent passages to understand the convection effect in turbulent flows. However, Taylor's model with a constant moving speed has many limitations, such as weak shear rates and low turbulence intensity [10,11]. In particular, due to ignorance of turbulent distortion, it incorrectly predicts the bandwidths of space-time energy spectra to be vanishing, that is to say, Taylor's frozen-flow hypothesis implies that the space-time energy spectrum is a one-dimensional curve, not a two-dimensional surface [see Fig. 1(a)]. This is in contradiction to the spreading ranges of energy spectra in frequency and wave number. Kraichnan [12] and Tennekes [13] proposed the random sweeping hypothesis to account for the distortion effect in homogeneous isotropic turbulence (HIT). The convection and distortion
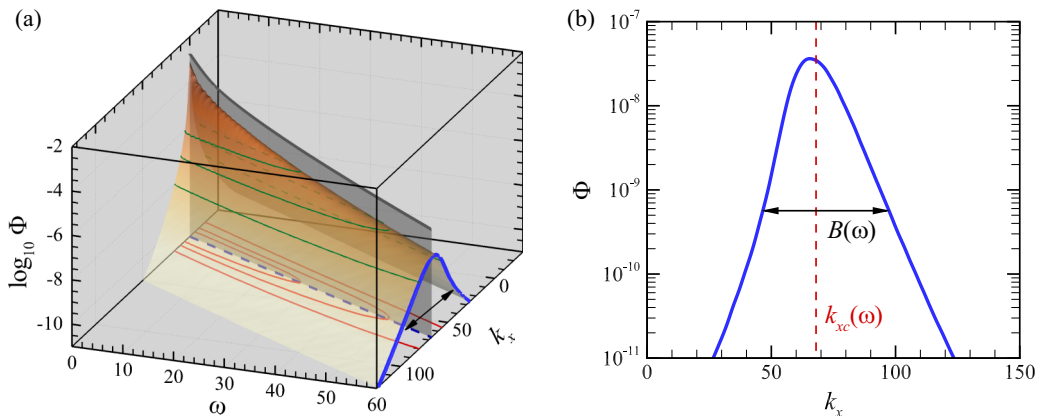
---

*hgw@lnm.imech.ac.cn

FIG. 1. Space-time energy spectrum $\Phi(k_x, \omega)$ of the streamwise velocity at $y^+ = 92$ obtained from DNS of turbulent channel flows at $\mathrm{Re}_\tau = 550$. (a) The colored surface shows the energy density in the frequency wave-number domain. The green lines denote the cuts of the surface with a fixed energy density. The red solid lines denote the isospectral contours that are approximately ellipses. The blue dashed line indicates the preferential direction of the contours, and its slope is related to the convection velocity. The blue solid line shows the spatial energy spectrum at a fixed frequency. For comparison, the space-time energy spectrum predicted by Taylor's model is represented by the gray curve, which exhibits vanishing spectral bandwidths. (b) The spatial energy spectrum at a fixed frequency (blue solid line) shown in panel (a) is plotted against wave numbers. The red dashed line denotes its mean wave number. The black solid line with arrows denotes its spectral bandwidth.

effects are also considered by treating the convection velocity as scale-dependent velocity [14] or superposition of mean velocity and random sweeping velocity [15–17]. We developed an elliptic approximation (EA) model [18,19] by using successive approximation to the contours of space-time correlation, which accounts for the coupling effect of convection and distortion.

We hope to develop simple stochastic models from the Navier-Stokes (NS) equations to reproduce space-time energy spectra. This can be achieved by decomposing the NS equations into a linear part and nonlinear terms: The linear part represents the dominating properties, and the nonlinear terms are modeled by random forcing. The random forcing is treated as an input in resolvent analysis [20–22] and input-output analysis [23,24] to reproduce the desired properties. White-in-time random forcing is conventionally used to predict the convection velocities [25] and geometric characteristics of energetic structures [26] in wall-bounded turbulence. However, white-in-time random forcing leads to divergent bandwidths of space-time energy spectra [27]. Colored-in-time random forcing is introduced to the resolvent analysis and input-output analysis, which improves the prediction of spectral bandwidths. Recently, we utilized dynamic autoregression (DAR) to determine random forcing [27]. The resultant DAR model can reproduce the space-time energy spectra with exact spectral bandwidths.

Reconstruction of space-time energy spectra requires a complete data set of turbulent fluctuations over spatial and temporal length scales. However, the data sets obtained from experimental measurements are often incomplete in the space and/or time domain. Taylor's model has been a staple tool to convert temporal spectra to spatial spectra in convection-dominating flows but fails in the reconstruction of space-time energy spectra [7]. Beall *et al.* [28] developed a local wave number (LW) model to improve the prediction. However, it still underpredicts the spectral bandwidths. de Kat and Ganapathisubramani [29] developed the frequency wave-number mapping approach to reconstruct space-time energy spectra. The local modulated wave (LMW) model [30] uses the local modulated wave to represent the wavelike structures in space and time and exactly predicts the spectral bandwidths.

The remainder of this article is organized as follows. In Sec. II, we review the phenomenological models for space-time energy spectra in turbulent shear flows. In Sec. III, we describe the random forcing approach for Taylor's model. The resultant DAR model can reproduce space-time energy spectra of exact mean frequencies and spectral bandwidths. In Sec. IV, we discuss how to use the incomplete data set from experimental measurements to reconstruct the space-time energy spectra. Finally, in Sec. V, we summarize the present understanding and physics-based models of space-time energy spectra and discuss future work.

II. PHENOMENOLOGICAL MODELS IN TERMS OF TURBULENT PASSAGE

A. Characterization of space-time energy spectra

In homogeneous turbulence, the space-time energy spectra $\Phi(\mathbf{k}, \omega)$ and the space-time correlations $R(\mathbf{r}, \tau)$ of velocity fluctuation are defined as

$$\Phi(\mathbf{k}, \omega) = \frac{1}{(2\pi)^4} \int R(\mathbf{r}, \tau) e^{-i(\mathbf{k}\cdot\mathbf{r}-\omega\tau)} d\mathbf{r} d\tau, \tag{1}$$

$$R(\mathbf{r}, \tau) = \langle u(\mathbf{x}, t) u(\mathbf{x} + \mathbf{r}, t + \tau) \rangle. \tag{2}$$

Here, $\Phi(\mathbf{k}, \omega)$ denotes the space-time energy spectra, $R(\mathbf{r}, \tau)$ denotes the space-time correlations, u is one component of the velocity field, $\mathbf{x} = (x, y, z)$ is the spatial coordinate, t is the temporal coordinate, $\mathbf{r} = (r_x, r_y, r_z)$ represents the spatial separation, τ represents the temporal separation, $\mathbf{k} = (k_x, k_y, k_z)$ is a three-dimensional wave-number vector, and ω is the frequency. The angular bracket $\langle \rangle$ denotes the ensemble averaging.

In turbulent channel flows, the velocity field is homogeneous in the streamwise (x) and spanwise (z) directions and inhomogeneous in the wall-normal direction (y). Accordingly, the space-time energy spectrum of the streamwise component u is defined on the x-z plane at location y, given by

$$\Phi(\boldsymbol{\kappa}, \omega; y) = \frac{1}{(2\pi)^3} \iiint R(r_x, r_z, \tau; y) e^{-i(k_x r_x + k_z r_z - \omega\tau)} dr_x dr_z d\tau, \tag{3}$$

$$R(r_x, r_z, \tau; y) = \langle u(x, y, z, t) u(x + r_x, y, z + r_z, t + \tau) \rangle, \tag{4}$$

where $\boldsymbol{\kappa} = (k_x, k_z)$ is a two-dimensional wave-number vector. k_x is the streamwise wave number, and k_z is the spanwise wave number. For convenience, the wall-normal location y in the independent variables is omitted, such that $\Phi(\boldsymbol{\kappa}, \omega; y)$ is simply written as $\Phi(\boldsymbol{\kappa}, \omega)$. Throughout this paper, the energy spectra are dependent on explicitly independent variables only. For example, $\Phi(k_x)$ refers to the spatial energy spectra with respect to the streamwise wave number, and $\Phi(k_x, \omega)$ refers to the space-time energy spectra with respect to the streamwise wave number and frequency.

The space-time energy spectra $\Phi(\boldsymbol{\kappa}, \omega)$ can be alternatively expressed through space-time Fourier modes $\tilde{u}(\boldsymbol{\kappa}, \omega)$ in terms of the Wiener-Khinchin theorem,

$$\Phi(\boldsymbol{\kappa}, \omega)\delta(\boldsymbol{\kappa} - \boldsymbol{\kappa}')\delta(\omega - \omega') = \langle \tilde{u}^*(\boldsymbol{\kappa}, \omega)\tilde{u}(\boldsymbol{\kappa}', \omega') \rangle, \tag{5}$$

where δ is the Dirac delta function. To study the decorrelation process, we introduce the time correlation $\Phi(\boldsymbol{\kappa}, \tau)$ of spatial Fourier mode $\hat{u}(\boldsymbol{\kappa}, t)$

$$\frac{\Phi(\boldsymbol{\kappa}, \tau)}{\Phi(\boldsymbol{\kappa})} = \frac{\langle \hat{u}^*(\boldsymbol{\kappa}, t)\hat{u}(\boldsymbol{\kappa}, t + \tau) \rangle}{\langle \hat{u}^*(\boldsymbol{\kappa}, t)\hat{u}(\boldsymbol{\kappa}, t) \rangle}, \tag{6}$$

which is related to space-time energy spectra through

$$\Phi(\boldsymbol{\kappa}, \omega) = \frac{1}{2\pi} \int \Phi(\boldsymbol{\kappa}, \tau) e^{i\omega\tau} d\tau. \tag{7}$$

Figure 1 shows the space-time energy spectrum of the streamwise velocity at $y^+ = 92$ obtained from the direct numerical simulation (DNS) of turbulent channel flows. The two-dimensional surface of the space-time energy spectrum is narrow and looks like a mountain. For comparison, the

space-time energy spectrum predicted by Taylor's model is represented by the gray curve, which exhibits vanishing spectral bandwidths. The isospectral contours (red solid lines) are approximately elliptic, which are similar to the isocorrelation contours. The two-dimensional surface decays most slowly along the ridge line and has a bell-shaped slice (blue solid line). The projection of the ridge line onto the frequency wave-number plane is the preference direction (blue dashed line) of the isospectral contours. Its slope is related to convection velocity. The width of the slice (black solid line with arrows) indicates the bandwidth of the space-time energy spectrum at a fixed frequency.

Spatial energy spectra and temporal energy spectra are the two marginal distributions of space-time energy spectra. In HIT, spatial energy spectra follow the $-5/3$ scaling with respect to wave numbers, and temporal energy spectra satisfy the same scaling, $-5/3$, with respect to frequencies [13]. In the log region of wall-bounded turbulence, in addition to the $-5/3$ scaling range, there may exist the range of scaling -1 [31–33] for the spatial and temporal marginal spectra. However, this scaling remains controversial in terms of the recent theoretical arguments and experimental measurements [14,29,34,35].

B. Conditional moments: mean and bandwidth

Space-time energy spectra describe the joint distribution of energy density over a broad range of frequencies and wave numbers. Analogous to probability distribution functions, they can be characterized by conditional moments at fixed frequencies or wave numbers.

(1) The first-order conditional moments at a fixed frequency give the mean wave number

$$k_{xc}(\omega) = \frac{\int k_x \Phi(k_x, \omega) dk_x}{\Phi(\omega)}. \tag{8}$$

The mean wave number $k_{xc}(\omega)$ can be used to calculate the frequency-dependent convection velocity, such as $c_u(\omega) = \omega/k_{xc}(\omega)$. It provides a statistical dispersion relation in turbulent flows [28].

(2) The second-order conditional moments at a fixed frequency give the spectral bandwidths

$$B(\omega) = \frac{\int (k_x - k_{xc})^2 \Phi(k_x, \omega) dk_x}{\Phi(\omega)}. \tag{9}$$

The nonzero spectral bandwidths describe spectral broadening in turbulent flows [11,36]: the energy density of small-scale eddies scatters around the statistical dispersion relation. In fact, small-scale eddies are distorted by large-scale shearing and small-scale interacting, rather than frozen without change.

The first- and second-order conditional moments can be used to investigate turbulent passage: the mean wave numbers are employed to calculate the propagation velocities of small-scale eddies, and the spectral bandwidths specify the extent of their distortion. The propagation velocities are used to describe the Doppler shift, and the spectral bandwidths are used to describe the Doppler broadening [11].

The temporal Fourier mode $\hat{u}(x, \omega)$ can be written in terms of its amplitude $a(x, \omega)$ and phase $\theta(x, \omega)$, such as

$$\hat{u}(x, \omega) = a(x, \omega)e^{i\theta(x,\omega)}. \tag{10}$$

We have the exact expressions for the mean wave numbers and the spectral bandwidth [37]:

$$k_{xc}(\omega) = \frac{\langle a^2 \partial_x \theta \rangle}{\langle a^2 \rangle}, \tag{11}$$

$$B(\omega) = \frac{\langle a^2(\partial_x \theta - k_{xc})^2 \rangle}{\langle a^2 \rangle} + \frac{\langle (\partial_x a)^2 \rangle}{\langle a^2 \rangle}. \tag{12}$$

EA model	Taylor ($V = 0$ in EA)	Kraichnan-Tennekes ($U = 0$ in EA)
$R(r,\tau) = R\left(\sqrt{(r - U\tau)^2 + V^2\tau^2}, 0\right)$	$R(r,\tau) = R\left(r - U\tau, 0\right)$	$R(r,\tau) = R\left(\sqrt{r^2 + V^2\tau^2}, 0\right)$

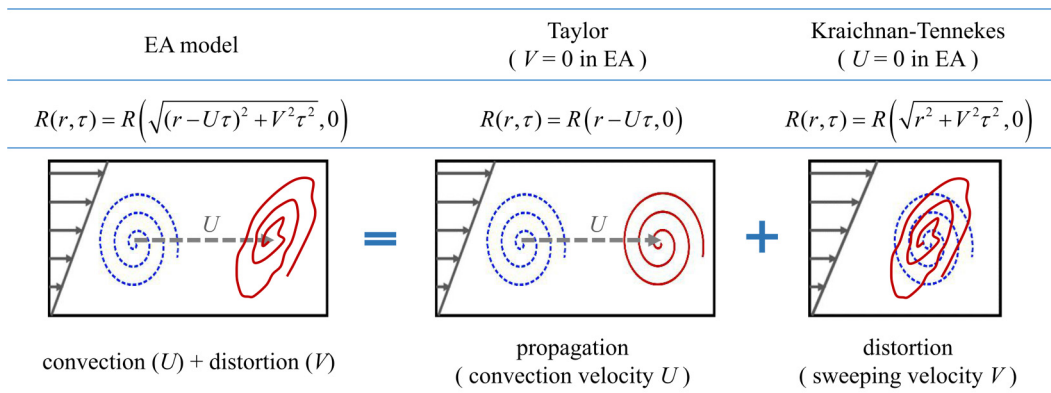| convection (U) + distortion (V) | propagation
(convection velocity U) | distortion
(sweeping velocity V) |

FIG. 2. Schematic representation of turbulent passage and the space-time correlation models. Turbulent passage is pictured as the downstream movement of flow patterns at a propagation speed with a certain distortion. In the EA model, space-time correlations are determined by the propagation and distortion of flow patterns. The former is represented by the propagation velocity U and the latter is represented by the sweeping velocity V. The EA model becomes Taylor's model if V is zero and becomes the Kraichnan-Tennekes random sweeping model if U is zero.

Equations (11) and (12) indicate that the mean wave number is determined by the phase derivative only, while the spectral bandwidth is determined by both the phase and amplitude derivatives. The DNS results [37] show that the contribution of the amplitude derivative to the spectral bandwidth is as important as that of the phase derivative and cannot be ignored in turbulent flows. Therefore, phase variation is not sufficient to describe spectral bandwidths. Taylor's model approximately reproduces the mean wave number. However, it incorrectly predicts the vanishing spectral bandwidths, since Taylor's model implies that the phase and amplitude are frozen and thus that both terms in the right-hand side of Eq. (12) are zero.

C. A picture of turbulent passage

Turbulent passage is pictured as the convection of small-scale eddies by large-scale eddies with distortion. In other words, small-scale eddies move downstream at a propagation speed with a certain distortion (see Fig. 2). Turbulent passage is dominated by the following three dynamic processes: the convection of small-scale eddies by large-scale eddies, the shearing of small-scale eddies by large-scale eddies, and the interaction of small-scale eddies. Both the interaction and the shearing distort small-scale eddies. The dynamic processes can be described by using phenomenological models: large-scale convection is represented by Taylor's model [9]; the contribution of the small-scale interaction to the time correlation is modeled by the Kraichnan-Tennekes random sweeping model [12,13]; and the contribution of the coupling effect of small-scale interaction and large-scale shearing to the time correlation is represented by the EA model [18,19].

Turbulent passage can be characterized by propagation velocity and sweeping velocity. The propagation velocity U of a generic variable q is defined as the value of convection velocity c which minimizes the square of the total derivative $\partial_t q + c\partial_x q$ [14]. Therefore, it gives the characteristic speed at which the small-scale eddies move downstream without distortion. This is the well-known Taylor's frozen-flow hypothesis. The sweeping velocity V is defined as the ensemble average of the square of the total derivative $\sigma \equiv \partial_t q + U \partial_x q$ normalized by the ensemble average of the square of the local derivative $\partial_x q$, where the convection velocity is taken as the propagation velocity U. As a result, it measures the deviation of Taylor's frozen flow $q(x - Ut)$ from the time-evolution flow $q(x, t)$, mainly due to the distortion of small-scale eddies.

The propagation velocity U and sweeping velocity V can be mathematically expressed as follows, respectively:

$$U = \arg\min_c \left\langle (\partial_t q + c \partial_x q)^2 \right\rangle = -\frac{\langle \partial_t q \partial_x q \rangle}{\langle (\partial_x q)^2 \rangle}, \tag{13}$$

$$V^2 = \frac{\langle \sigma^2 \rangle}{\langle (\partial_x q)^2 \rangle} = \frac{\left\langle (\partial_t q + U \partial_x q)^2 \right\rangle}{\langle (\partial_x q)^2 \rangle}, \tag{14}$$

where arg min denotes the argument of the minimum. Physically, the propagation velocity is referred to as the speed of downstream movement of small-scale eddies. The sweeping velocity is referred to as the variation velocity of small-scale eddies of the characteristic length scale $\sqrt{\langle q^2 \rangle / \langle (\partial_x q)^2 \rangle}$ at the Taylor time microscale $\sqrt{\langle q^2 \rangle / \langle \sigma^2 \rangle}$ in the moving frame at the propagation speed U. Therefore, the sweeping velocity characterizes the distortion of small-scale eddies caused by large-scale shearing and small-scale interaction. The sweeping velocity used in the present study is completely different from the similar term "sweep" in wall-bounded turbulent flows: The former is referred to as the characteristic velocity which specifies the decorrelation rapidity of small scale eddies; the latter is referred to as the flow event toward the wall which leads to local acceleration of the streamwise component in turbulent boundary layers [38].

According to the mean frequency and spectral bandwidth, the propagation and sweeping velocities can be rewritten as [27]

$$U = \frac{\int c_u(k_x) k_x^2 \Phi(k_x) dk_x}{\int k_x^2 \Phi(k_x) dk_x}, \tag{15}$$

$$V^2 = \frac{\int B(k_x) \Phi(k_x) dk_x}{\int k_x^2 \Phi(k_x) dk_x} + \left\{ \frac{\int c_u^2(k_x) k_x^2 \Phi(k_x) dk_x}{\int k_x^2 \Phi(k_x) dk_x} - \left[\frac{\int c_u(k_x) k_x^2 \Phi(k_x) dk_x}{\int k_x^2 \Phi(k_x) dk_x} \right]^2 \right\}, \tag{16}$$

where $c_u(k_x) = \omega_c(k_x)/k_x$ is a wave-number-dependent convection velocity. Equation (15) implies that the propagation velocity is the weighted average of wave-number-dependent convection velocities [14]. In Eq. (16), the sweeping velocity is the sum of two terms: The first term represents the contribution of the spectral bandwidths, and the second term represents the contribution of the wave-number-dependent convection velocities. This implies that the wave-number-dependent convection velocities alone cannot produce the correct sweeping velocity.

In HIT, the propagation and sweeping velocities for the fluctuating velocity vector $\mathbf{u} = (u_1, u_2, u_3)$ can be respectively expressed as follows:

$$U = \arg\min_c \left\langle (\partial_t u_i + c \partial_x u_i)^2 \right\rangle = -\frac{\langle \partial_t u_i \partial_x u_i \rangle}{\langle \partial_x u_i \partial_x u_i \rangle}, \tag{17}$$

$$V^2 = \frac{\langle \sigma_i \sigma_i \rangle}{\langle \partial_x u_i \partial_x u_i \rangle} = \frac{\left\langle (\partial_t u_i + U \partial_x u_i)^2 \right\rangle}{\langle \partial_x u_i \partial_x u_i \rangle}, \tag{18}$$

where $\sigma_i \equiv \partial_t u_i + U \partial_x u_i$ $(i = 1, 2, 3)$. The repeated indices imply the Einstein summation convention. According to the Kraichnan-Tennekes random sweeping hypothesis [12,13], we have

$$\sigma_i = -\mathbf{v} \cdot \nabla u_i = -(v_1 \partial_x u_i + v_2 \partial_y u_i + v_3 \partial_z u_i), \tag{19}$$

where the random velocity $\mathbf{v} = (v_1, v_2, v_3)$ satisfies a Gaussian distribution of zero mean and the correlation $\langle v_i v_j \rangle = \langle \mathbf{u}^2 \rangle \delta_{ij}/3$. Moreover, $\mathbf{v}$ is independent of $\mathbf{u}$ and constant in both space and time. Hence, the sweeping velocity can be calculated through

$$V^2 = \frac{\langle \sigma_i \sigma_i \rangle}{\langle \partial_x u_i \partial_x u_i \rangle} = \langle v_1^2 \rangle + \langle v_2^2 \rangle + \langle v_3^2 \rangle = \langle \mathbf{u}^2 \rangle. \tag{20}$$

Therefore, the value of the sweeping velocity V in HIT is the rms of the fluctuating velocity vector **u**. Kraichnan proposed that the sweeping velocity in HIT can be treated as a random convection velocity, which has been justified theoretically and verified numerically [1].

In homogeneous shear turbulence, the propagation velocity is simply taken as $U = U_1$, where U_1 is the mean velocity. If the pressure and viscous terms are ignorable, we have

$$\sigma_i = -\mathbf{v} \cdot \nabla u_i - \delta_{i1} S u_2, \tag{21}$$

where S is a mean shear rate. Therefore, since the fluctuating velocity **u** is assumed to be isotropic, the sweeping velocity is given by

$$V^2 = \langle v_1^2 \rangle + \langle v_2^2 \rangle \frac{\langle \partial_y u_i \partial_y u_i \rangle}{\langle \partial_x u_i \partial_x u_i \rangle} + \langle v_3^2 \rangle \frac{\langle \partial_z u_i \partial_z u_i \rangle}{\langle \partial_x u_i \partial_x u_i \rangle} + \frac{S^2 \langle u_2^2 \rangle}{\langle \partial_x u_i \partial_x u_i \rangle} = \langle \mathbf{u}^2 \rangle + S^2 \lambda_T^2, \tag{22}$$

where $\lambda_T = \sqrt{\langle u_i u_i \rangle / \langle \partial_j u_i \partial_j u_i \rangle}$ is the Taylor length microscale [19].

The turbulent passage has been used to understand space-time energy spectra. For example, large-scale convection causes a Doppler shift, and small-scale distortion causes Doppler broadening [11]. It has also been used to study the temporal decorrelation in turbulent shear flows: Time correlation is mainly determined by small-scale interaction and large-scale shearing. Turbulent passage serves as a supplement to the energy cascade process to investigate the spatiotemporal dynamics of turbulent flows.

D. Taylor, Kraichnan-Tennekes, and EA models

In this subsection, we briefly review the Taylor [9], Kraichnan-Tennekes [12,13], and EA [18,19] models of space-time correlations in terms of the successive approximation to isocorrelation contours. The obtained results are consistent with the turbulent passage picture. Throughout this subsection, $R(r, \tau)$ refers to the sum of the correlations of all velocity components, and $\Phi(k_x, \omega)$ refers to the sum of the energy spectra of all velocity components.

The numerical simulations and experimental measurements show that the isocorrelation contours are elongated and closed curves with a preferential direction. The second approximation to the isocorrelation contours leads to an EA model, given by

$$R(r, \tau) = R\left(\sqrt{(r - U\tau)^2 + V^2 \tau^2}, 0\right). \tag{23}$$

Here, the parameters U and V can be determined by using the Taylor expansion of $R(r, \tau)$, which yields

$$U = -\left. \frac{\partial_{r\tau}^2 R(r, \tau)}{\partial_{rr}^2 R(r, \tau)} \right|_{r=0 \ \tau=0}, \tag{24}$$

$$V^2 = \left. \frac{\partial_{\tau\tau}^2 R(r, \tau)}{\partial_{rr}^2 R(r, \tau)} \right|_{r=0 \ \tau=0} - U^2. \tag{25}$$

It is shown that the parameters U and V in Eqs. (24) and (25) are consistent with those in Eqs. (17) and (18). Therefore, U is the propagation velocity and V is the sweeping velocity. The EA model implies that the space-time correlation is determined by spatial correlation and the nonlinear transform of elliptic form. The EA model becomes Taylor's model $R(r, \tau) = R(r - U\tau, 0)$ if $V = 0$, and it becomes the Kraichnan-Tennekes random sweeping model $R(r, \tau) = R(\sqrt{r^2 + V^2\tau^2}, 0)$ up to a second-order approximation if $U = 0$.

The EA model is consistent with the turbulent passage picture. In homogeneous shear flows, the propagation and sweeping velocities can be expressed as $U = U_1$ and $V^2 = \langle \mathbf{u}^2 \rangle + S^2 \lambda_T^2$, respectively [19]. The propagation velocity represents the large-scale convection effect; the first term in V^2 represents the small-scale interaction effect and the second term represents the large-scale shearing effect. Taylor's model is the first approximation of the iso-correlation contours, since its

iso-correlation contours are straight lines, $r - U\tau =$ const. In this case, the mean frequencies and spectral bandwidths are $\omega_c(k_x) = k_x U$ and $B(k_x) = 0$, respectively. Moreover, in the Kraichnan-Tennekes random sweeping model, the mean frequencies and spectral bandwidths are $\omega_c(k_x) = 0$ and $B(k_x) = \iint k^2 \mathrm{v}^2 \Phi(\mathbf{k}) dk_y dk_z / \iint \Phi(\mathbf{k}) dk_y dk_z$, respectively, where $\mathrm{v}^2 = V^2/3$ is the variance of one velocity component. This model predicts the spectral bandwidths in HIT.

III. STOCHASTIC DYNAMIC MODELS

This section is devoted to reviewing stochastic dynamic models for space-time energy spectra of velocity fluctuations. The governing equations of velocity fluctuations about laminar or turbulent base flows can be decomposed into a linear part and a nonlinear term. The linear part without the nonlinear term simply corresponds to the linearized NS equations (LNSEs). In resolvent analysis and input-output analysis, the nonlinear term plays a role of nonlinear forcing, which can be treated as random forcing. The problem is how to model the nonlinear forcing to generate the desired properties of turbulent fluctuations. We discuss white random forcing in Sec. III A and colored random forcing in Sec. III B. In the recently developed DAR model, the nonlinear forcing is modeled by using stochastic dynamic equations, where the LNSEs are simplified as Taylor's model. The DAR forcing is discussed in Sec. III C.

In the framework of resolvent analysis and input-output analysis, the space-time energy spectra are related to nonlinear forcing. LNSEs with a forcing in turbulent channel flows can be conceptually written as

$$\frac{\partial \hat{\mathbf{q}}}{\partial t} = \mathbf{A}\hat{\mathbf{q}} + \mathbf{B}\hat{\mathbf{F}}. \tag{26}$$

Here, $\hat{\mathbf{q}}(\boldsymbol{\kappa}, t)$ is the state vector, such as $[\hat{u}\ \hat{v}\ \hat{w}\ \hat{p}]^T$, $[\hat{v}\ \hat{\omega}_y]^T$ or simply one velocity component $\hat{u}$. In addition, $\hat{u}$, $\hat{v}$, and $\hat{w}$ are the velocity fluctuations in the streamwise, wall-normal, and spanwise directions, respectively; $\hat{p}$ is the pressure fluctuation; and $\hat{\omega}_y$ is the wall-normal vorticity. $\mathbf{A}(\boldsymbol{\kappa})$ is a linear operator. $\hat{\mathbf{F}}(\boldsymbol{\kappa}, t)$ represents nonlinear forcing. $\mathbf{B}(\boldsymbol{\kappa})$ modifies the nonlinear forcing such that it maps the nonlinear forcing to the excitations.

Equation (26) can be written in the frequency domain

$$-i\omega\tilde{\mathbf{q}} = \mathbf{A}\tilde{\mathbf{q}} + \mathbf{B}\tilde{\mathbf{F}}, \tag{27}$$

which gives the solution

$$\tilde{\mathbf{q}} = \mathbf{R}\mathbf{B}\tilde{\mathbf{F}} \equiv (-i\omega\mathbf{I} - \mathbf{A})^{-1}\mathbf{B}\tilde{\mathbf{F}}, \tag{28}$$

where $\tilde{\mathbf{q}}(\boldsymbol{\kappa}, \omega)$ and $\tilde{\mathbf{F}}(\boldsymbol{\kappa}, \omega)$ are the temporal Fourier transformations of $\hat{\mathbf{q}}$ and $\hat{\mathbf{F}}$, respectively, and $\mathbf{R} = (-i\omega\mathbf{I} - \mathbf{A})^{-1}$ is the resolvent operator [20–22]. Therefore, the space-time spectrum of the state vector $\tilde{\mathbf{q}}$ is given by

$$\boldsymbol{\Phi}_{\tilde{\mathbf{q}}}(\boldsymbol{\kappa}, \omega) \equiv \langle \tilde{\mathbf{q}}\tilde{\mathbf{q}}^* \rangle = \mathbf{R}\mathbf{B}\langle \tilde{\mathbf{F}}\tilde{\mathbf{F}}^* \rangle \mathbf{B}^*\mathbf{R}^* \equiv \mathbf{R}\mathbf{B}\boldsymbol{\Phi}_{\tilde{\mathbf{F}}}(\boldsymbol{\kappa}, \omega)\mathbf{B}^*\mathbf{R}^*, \tag{29}$$

where $\boldsymbol{\Phi}_{\tilde{\mathbf{q}}}$ is the space-time cross spectrum of the state vector and $\boldsymbol{\Phi}_{\tilde{\mathbf{F}}}$ is the space-time cross spectrum of the forcing. In input-output analysis [24,39], a linear operator $\mathbf{C}(\boldsymbol{\kappa})$ can be used to extract the desired quantities from $\tilde{\mathbf{q}}$, which provides a general framework.

A. White random forcing

The application of white random forcing to LNSEs can reproduce certain characteristics of coherent structures in transition and turbulence (e.g., wall-bounded turbulence and free shear turbulence). However, it will be shown that white-in-time random forcing generates a divergent spectral bandwidth (see the final part of this subsection), which implies vanishing Taylor microscales in time.

Farrell and Ioannou [26] introduced white-in-time random forcing into LNSEs to show transient amplification in the laminar-turbulent transition. The whiteness in time leads to the dominant forcing modes being conveniently obtained from the eigenvectors of the solution of a Lyapunov equation. On the other hand, the resolvent response modes correspond to the spectral POD (SPOD) modes subject to white-in-space random forcing [40,41]. Schmidt *et al.* [42] and Lesshafft *et al.* [43] numerically showed good agreement between the leading SPOD modes and the optimal resolvent response modes in turbulent jets.

The random forcing that is white in both time and space has been used for spatiotemporal properties. Farrell and Ioannou [44] introduced a finite coherence timescale into the solution of LNSEs subject to spatiotemporally white forcing. This system gives the space-time energy spectra in premultiplied form whose wave number and frequency at peak are consistent with the experimental measurements. Spatiotemporally white forcing is also introduced into the LNSEs in the frame of input-output analysis [45]. The obtained results show that the energy amplification of the streamwise constant perturbations in channel flows is scaled as $O(\mathrm{Re}^3)$. In Jovanović and Bamieh's paper [39], spatiotemporally white forcing is used as an input to investigate the componentwise energy amplification, and the optimal outputs are the streamwise vortices and streaks, oblique waves, and Tollmien-Schlichting waves. Liu and Gayme [25] used spatiotemporally white forcing as inputs and computed the space-time energy spectra through the input-output operator in turbulent channel flows. They demonstrated that the convection velocities estimated from the obtained space-time energy spectra are in good agreement with the DNS results in the literature [46,47].

However, we can show that the white-in-time random forcing in Eq. (26) leads to divergent spectral bandwidth. For simplicity, $\mathbf{B}(\boldsymbol{\kappa})$ is taken as an identity operator, and $\hat{\mathbf{F}}(\boldsymbol{\kappa}, t)$ is taken as white-in-time random forcing with its intensity $\boldsymbol{\Phi}_{\hat{\mathbf{F}}}(\boldsymbol{\kappa})$, such that $\langle \hat{\mathbf{F}}(\boldsymbol{\kappa}, t)\hat{\mathbf{F}}^*(\boldsymbol{\kappa}, t')\rangle = \boldsymbol{\Phi}_{\hat{\mathbf{F}}}(\boldsymbol{\kappa})\delta(t - t')$. The solution of Eq. (26) can be written as

$$\hat{\mathbf{q}}(\boldsymbol{\kappa}, t) = \int_{-\infty}^{t} e^{(t-s)\mathbf{A}}\hat{\mathbf{F}}(\boldsymbol{\kappa}, s)ds, \tag{30}$$

which yields

$$\langle \hat{\mathbf{q}}(\boldsymbol{\kappa}, t)\hat{\mathbf{F}}^*(\boldsymbol{\kappa}, t)\rangle = \langle \hat{\mathbf{F}}(\boldsymbol{\kappa}, t)\hat{\mathbf{q}}^*(\boldsymbol{\kappa}, t)\rangle = \boldsymbol{\Phi}_{\hat{\mathbf{F}}}(\boldsymbol{\kappa})/2. \tag{31}$$

Therefore, $\langle \hat{\mathbf{q}}(\boldsymbol{\kappa}, t)\hat{\mathbf{F}}^*(\boldsymbol{\kappa}, t)\rangle$ and $\langle \hat{\mathbf{F}}(\boldsymbol{\kappa}, t)\hat{\mathbf{q}}^*(\boldsymbol{\kappa}, t)\rangle$ are finite. According to Eq. (26), we obtain

$$\langle \hat{\mathbf{q}}\partial_t\hat{\mathbf{q}}^*\rangle = \langle \hat{\mathbf{q}}(\boldsymbol{\kappa}, t)\hat{\mathbf{q}}^*(\boldsymbol{\kappa}, t)\rangle \mathbf{A}^* + \langle \hat{\mathbf{q}}(\boldsymbol{\kappa}, t)\hat{\mathbf{F}}^*(\boldsymbol{\kappa}, t)\rangle \tag{32}$$

and

$$\langle \partial_t\hat{\mathbf{q}}\partial_t\hat{\mathbf{q}}^*\rangle = \mathbf{A}\langle \hat{\mathbf{q}}(\boldsymbol{\kappa}, t)\hat{\mathbf{q}}^*(\boldsymbol{\kappa}, t)\rangle \mathbf{A}^* + \mathbf{A}\langle \hat{\mathbf{q}}(\boldsymbol{\kappa}, t)\hat{\mathbf{F}}^*(\boldsymbol{\kappa}, t)\rangle + \langle \hat{\mathbf{F}}(\boldsymbol{\kappa}, t)\hat{\mathbf{q}}^*(\boldsymbol{\kappa}, t)\rangle \mathbf{A}^* + \langle \hat{\mathbf{F}}(\boldsymbol{\kappa}, t)\hat{\mathbf{F}}^*(\boldsymbol{\kappa}, t)\rangle. \tag{33}$$

All of the terms in the right-hand side of Eq. (32) are of finite values. As a result, $\langle \hat{\mathbf{q}}\partial_t\hat{\mathbf{q}}^*\rangle$ is finite. However, the term $\langle \hat{\mathbf{F}}(\boldsymbol{\kappa}, t)\hat{\mathbf{F}}^*(\boldsymbol{\kappa}, t)\rangle$ in the right-hand side of Eq. (33) is divergent. Hence, $\langle \partial_t\hat{\mathbf{q}}\partial_t\hat{\mathbf{q}}^*\rangle$ is divergent. Therefore, there exists at least one component $\hat{q}(\boldsymbol{\kappa}, t)$ in $\hat{\mathbf{q}}(\boldsymbol{\kappa}, t)$ such that $\langle \partial_t\hat{q}\partial_t\hat{q}^*\rangle$ is divergent.

In terms of their definitions, we can calculate the mean frequency and spectral bandwidth

$$\frac{\langle \hat{q}\partial_t\hat{q}^*\rangle}{\langle \hat{q}\hat{q}^*\rangle} = i\omega_c(\boldsymbol{\kappa}), \tag{34}$$

$$\frac{\langle \partial_t\hat{q}\partial_t\hat{q}^*\rangle}{\langle \hat{q}\hat{q}^*\rangle} = B(\boldsymbol{\kappa}) + \omega_c^2(\boldsymbol{\kappa}). \tag{35}$$

Equation (34) implies that $\omega_c(\boldsymbol{\kappa})$ is finite. However, the divergent $\langle \partial_t\hat{q}\partial_t\hat{q}^*\rangle/\langle \hat{q}\hat{q}^*\rangle$ in Eq. (35) implies that $B(\boldsymbol{\kappa})$ is divergent, resulting in vanishing Taylor microscales [27].

B. Colored random forcing

Numerical simulations of turbulent shear flows show that the nonlinear terms in the NS equations are not white in either space or time. Towne *et al.* [48] found that the nonlinear forcing is spatially coherent in a jet, although its coherence length scales are smaller than the flow pressure. They further proposed a fit function for the cross spectra of the forcing in the high-Reynolds-number jet. Nogueira *et al.* [49] showed that white-in-space random forcing leads to velocity responses inconsistent with DNS results in turbulent Couette flows. In fact, the nonlinear forcing exhibits coherent structures, such as a streamwise vortex in the forcing and a destructive interference between the lift-up mechanism and the streamwise forcing. In turbulent channel flows, Morra *et al.* [50] demonstrated that the nonlinear forcing is colored-in-time since there exists a peak in the frequency spectra of the nonlinear forcing for buffer-layer structures and large-scale motions. They also found that the spatial coherent structures of the nonlinear forcing are in agreement with the results in Nogueira *et al.* [49].

The coherence of nonlinear forcing suggests that colored random forcing is necessarily introduced for reproducing the spatiotemporal properties of turbulent flows. Rosenberg *et al.* [51] used the triadic interaction of velocity modes to represent the nonlinear forcing [22,52], where only dominant energetic modes are taken into account and estimated from the resolvent optimal response modes. Moarref *et al.* [53] proposed a resolvent-based low-order decomposition in the determination of nonlinear forcing. In turbulent channel flows, the velocity is expressed as a weighted sum of resolvent response modes, where the weights represent the projection of the nonlinear forcing onto the resolvent forcing modes. The weights are determined by using a convex optimization scheme to minimize the errors between the spatial spectra from the resolvent-based low-order representation of velocity fields and the DNS results. Furthermore, McMullen *et al.* [54] used the Orr-Sommerfeld and Squire decomposition to replace the resolvent-based decomposition. The interesting result is that the obtained spectrum can capture most of the energetic content in the frequency wave-number plane even if only a spatial energy spectrum is used to determine the nonlinear forcing.

Zare *et al.* [23,55] showed that a white-in-time random forcing cannot reproduce the spatial cross spectra of velocity fluctuations in turbulent channel flows and thus proposed colored-in-time random forcing instead. Here, the colored-in-time random forcing is expressed as the sum of a white-in-time forcing and a dynamical filter of the white-in-time forcing. It is obtained by using an optimization algorithm for the maximal entropy and the low complexity to match the known spatial energy spectra at all locations in the wall-normal direction. The colored-in-time forcing is further shown to be equivalent to the modification of LNSEs with a white-in-time forcing. This method can predict the spatial cross spectra and convection velocities of velocity fluctuations.

Morra *et al.* [56] used the eddy-viscosity-enhanced random forcing to estimate the space-time cross spectra of the buffer-layer structure and large-scale motions in turbulent channel flows. The eddy-viscosity-enhanced forcing can be the sum of the eddy viscosity and white random forcing. The eddy viscosity is widely used in LNSEs and the resolvent analysis [57–65] and is represented by the Cess model [66,67] in turbulent channel flows. The obtained space-time energy spectra and cross spectra at several fixed wave numbers are in better agreement with the DNS results, since the projections of the eddy-viscosity-enhanced random forcing onto the resolvent forcing modes are closer to the DNS results [50].

Towne *et al.* [68] used the eddy-viscosity-enhanced resolvent operator to estimate the space-time correlation in the inner layer of turbulent channel flows. The random forcing is determined to reproduce the known space-time cross spectra at one location in the outer layer with its minimal norm, where the pseudoinverse of the componentwise resolvent operator is taken. In turbulent channel flows, the location at $y^+ = 37$ is taken for reconstructing the random forcing. It is used to predict the spatial spectra, temporal spectra, space-time cross-spectra, and convection velocity. The convection velocity extracted from the estimated space-time correlation is consistent with the DNS result. This approach [68] was further extended by introducing sensor noise in the framework

of a Wiener filter [69]. Yang *et al.* [70] found that the location of the known input data is critically important to the results.

C. Dynamic autoregressive (DAR) forcing

In the DAR models, LNSEs are simplified as Taylor's model. The nonlinear forcing is estimated by using the dynamic autoregression method, which leads to stochastic dynamic equations. The DAR model for the streamwise velocity component at a fixed wall-normal location is given by [27]

$$\underbrace{\frac{\partial \hat{u}(\boldsymbol{\kappa}, t)}{\partial t} = -i k_x U_c \hat{u}(\boldsymbol{\kappa}, t)}_{\text{Taylor's model}} + \underbrace{\hat{\sigma}(\boldsymbol{\kappa}, t)}_{\text{DAR forcing}}, \tag{36a}$$

$$\frac{\partial \hat{\sigma}(\boldsymbol{\kappa}, t)}{\partial t} = \underbrace{-i k_x U_c \hat{\sigma}(\boldsymbol{\kappa}, t)}_{\text{convection}} \underbrace{- b(\boldsymbol{\kappa}) \hat{u}(\boldsymbol{\kappa}, t)}_{\text{random sweeping}} \underbrace{- 2 q(\boldsymbol{\kappa}) \hat{\sigma}(\boldsymbol{\kappa}, t)}_{\text{damping}} + \underbrace{\sqrt{2 b(\boldsymbol{\kappa}) q(\boldsymbol{\kappa}) \Phi(\boldsymbol{\kappa})} \hat{\xi}(\boldsymbol{\kappa}, t)}_{\text{white}-\text{in}-\text{time forcing}}. \tag{36b}$$

Here, U_c is the convection velocity. $b(\boldsymbol{\kappa}) \approx k_x^2 V_x^2 + k_z^2 V_z^2$ determines the spectral bandwidth, where V_x and V_z are the streamwise and spanwise sweeping velocities, respectively. $q(\boldsymbol{\kappa}) = \sqrt{b(\boldsymbol{\kappa})}$ is the damping coefficient; $\hat{\xi}(\boldsymbol{\kappa}, t)$ is a complex white-in-time random forcing given by $\langle \hat{\xi}^*(\boldsymbol{\kappa}, t) \hat{\xi}(\boldsymbol{\kappa}', t') \rangle = 2\delta(\boldsymbol{\kappa} - \boldsymbol{\kappa}')\delta(t - t')$. $\Phi(\boldsymbol{\kappa})$ is the spatial energy spectrum of the velocity $\hat{u}(\boldsymbol{\kappa}, t)$ and specifies the amplitude of the white-in-time random forcing.

In the DAR model, the evolution of the velocity component is governed by Taylor's model subject to a DAR forcing. The DAR forcing is determined by large-scale convection, random sweeping, damping, and white-in-time noise, as shown in Eq. (36b). Therefore, the DAR model is consistent with the picture of turbulent passage. In fact, the derivation of the DAR model is based on the picture of turbulent passage by using dynamic autoregression.

The temporal correlations of velocity modes can be obtained from the DAR model

$$\Phi(\boldsymbol{\kappa}, \tau) = \Phi(\boldsymbol{\kappa})(1 + \sqrt{b(\boldsymbol{\kappa})}|\tau|)e^{-\sqrt{b(\boldsymbol{\kappa})}|\tau| - i k_x U_c \tau}, \tag{37}$$

which gives the space-time energy spectra

$$\Phi(\boldsymbol{\kappa}, \omega) = \Phi(\boldsymbol{\kappa}) \frac{2 b^{3/2}(\boldsymbol{\kappa})}{\pi [(\omega - k_x U_c)^2 + b(\boldsymbol{\kappa})]^2}. \tag{38}$$

The most important observation is that the space-time energy spectra give the conditional mean frequencies and spectral bandwidths as follows:

$$\omega_c(\boldsymbol{\kappa}) = \frac{\int \omega \Phi(\boldsymbol{\kappa}, \omega) d\omega}{\Phi(\boldsymbol{\kappa})} = k_x U_c \tag{39}$$

and

$$B(\boldsymbol{\kappa}) = \frac{\int (\omega - \omega_c)^2 \Phi(\boldsymbol{\kappa}, \omega) d\omega}{\Phi(\boldsymbol{\kappa})} = b(\boldsymbol{\kappa}) = k_x^2 V_x^2 + k_z^2 V_z^2. \tag{40}$$

The mean frequencies are the same as those in Taylor's model, and the spectral bandwidths are the same as those in the Kraichnan-Tennekes model. In particular, the spectral bandwidth at k_x is given by [27]

$$B(k_x) = k_x^2 V_x^2 + V_z^2 \frac{\int k_z^2 \Phi(\boldsymbol{\kappa}) dk_z}{\int \Phi(\boldsymbol{\kappa}) dk_z}. \tag{41}$$

In the DAR model, the inputs are spatial energy spectra and three parameters: convection velocity U_c and streamwise and spanwise sweeping velocities, V_x and V_z. These parameters can
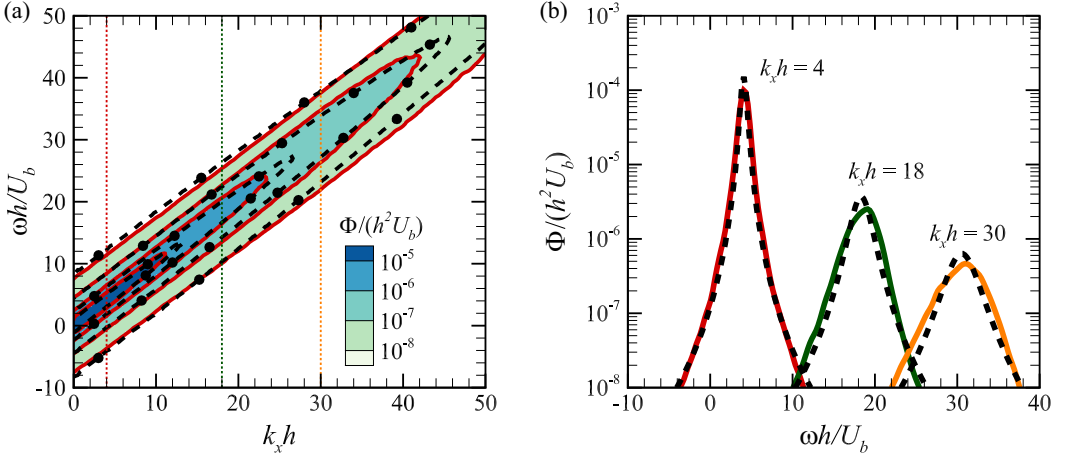
FIG. 3. Comparison of the space-time energy spectra obtained from the DNS and the DAR model for the streamwise velocity fluctuations at $y^+ = 270$ in turbulent channel flows at $\text{Re}_\tau = 550$. (a) Contours obtained from the DNS (colored shades with solid lines) and the DAR model (dashed lines with dots). (b) Cuts through space-time energy spectra at three different wave numbers obtained from the DNS (colored solid lines) and the DAR model (dashed lines). Figure adapted from Ref. [27].

be determined by matching with the EA model at small spatial and temporal separations, which are given by

$$U_c = \frac{\int c_u(k_x) k_x^2 \Phi(k_x) dk_x}{\int k_x^2 \Phi(k_x) dk_x}, \tag{42}$$

$$V_z^2 = \left. \frac{B(k_x) \int \Phi(\boldsymbol{\kappa}) dk_z}{\int k_z^2 \Phi(\boldsymbol{\kappa}) dk_z} \right|_{k_x=0}, \tag{43}$$

$$V_x^2 = \frac{\int B(k_x) \Phi(k_x) dk_x}{\int k_x^2 \Phi(k_x) dk_x} - V_z^2 \frac{\int k_z^2 \Phi(k_z) dk_z}{\int k_x^2 \Phi(k_x) dk_x}. \tag{44}$$

The convection velocity in Eq. (42) is obtained from Eq. (15). The spanwise sweeping velocity V_z in Eq. (43) is obtained from Eq. (41) at $k_x = 0$. The streamwise sweeping velocity V_x is obtained by substituting Eq. (41) into the average of the spectral bandwidth $B(k_x)$ with the weight $\Phi(k_x)/\int k_x^2 \Phi(k_x) dk_x$. The parameters U_c, V_x, and V_z in the DAR model are different at different wall-normal locations, since the wave-number-dependent convection velocity $c_u(k_x)$, the spectral bandwidth $B(k_x)$, and the spatial energy spectra are dependent on the wall-normal locations.

The DAR model is applied to the streamwise velocity fluctuations in turbulent channel flows at $\text{Re}_\tau = 550$ [27]. The bulk Reynolds number $\text{Re} \equiv U_b h/\nu$ is approximately 10 000, where h is the channel half-height, U_b is the bulk velocity, and ν is the kinematic viscosity. Figure 3 compares the space-time energy spectra and the temporal spectra at different wave numbers obtained from the DNS and the DAR model at $y^+ = 270$. The line contours from the DAR model are in good agreement with those from the DNS.

To reproduce the space-time energy spectra and wave-number-dependent convection velocities in the near-wall region, linear stochastic estimation (LSE) [71] is employed to represent the large-scale motions, which leads to

$$\hat{u}^{\text{L}}(\boldsymbol{\kappa}, t; y_W) = \alpha(\boldsymbol{\kappa}; y_W, y_O) \hat{u}(\boldsymbol{\kappa}, t; y_O) \tag{45}$$
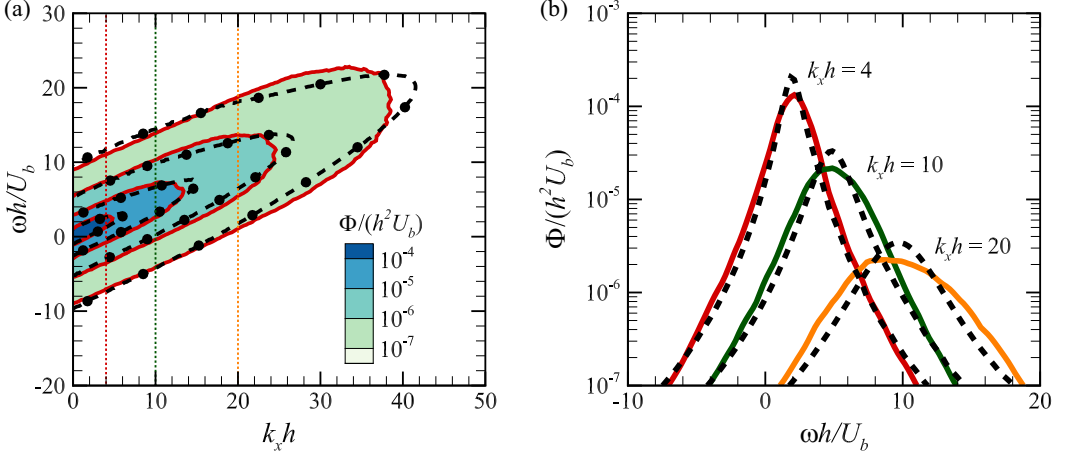
FIG. 4. Comparison of the space-time energy spectra obtained from the DNS and the DAR model with LSE for the streamwise velocity fluctuations at $y^+ = 5$ in turbulent channel flows at $\mathrm{Re}_\tau = 550$. (a) Contours obtained from the DNS (colored shades with solid lines) and the DAR model (dashed lines with dots). (b) Cuts through space-time energy spectra at three different wave numbers obtained from the DNS (colored solid lines) and the DAR model (dashed lines). Figure adapted from Ref. [27].

and

$$\alpha(\kappa; y_W, y_O) = \frac{\langle \hat{u}^*(\kappa, t; y_O)\hat{u}(\kappa, t; y_W)\rangle}{\langle \hat{u}^*(\kappa, t; y_O)\hat{u}(\kappa, t; y_O)\rangle}, \tag{46}$$

where $\hat{u}^{\mathrm{L}}(\kappa, t; y_W)$ is the large-scale motion at the near-wall location y_W and $\hat{u}(\kappa, t; y_O)$ is the velocity at the location y_O in the outer layer. The correlation of the spatial Fourier modes between the near-wall location y_W and outer-layer location y_O, $\langle \hat{u}^*(\kappa, t; y_O)\hat{u}(\kappa, t; y_W)\rangle$, is used to calculate $\alpha(\kappa; y_W, y_O)$. Therefore, the remaining part of the near-wall velocity fluctuations is given by

$$\hat{u}^{\mathrm{R}}(\kappa, t; y_W) = \hat{u}(\kappa, t; y_W) - \hat{u}^{\mathrm{L}}(\kappa, t; y_W). \tag{47}$$

The DAR model is used to generate the small-scale motions that have the space-time energy spectra of the remaining part $\hat{u}^{\mathrm{R}}$, in which the parameters $\Phi(\kappa)$, U_c, V_x, and V_z are determined from the remaining part by using Eqs. (42), (43), and (44). In fact, the DAR model is able to generate the small-scale motions of the correct spectral bandwidths in the near-wall region. However, the parameter U_c in the DAR model is taken as a constant and thus cannot represent the wave-number dependence of the convection velocity. Therefore, the combination of DAR and LSE is used to reproduce the wave-number-dependent convection velocity consistent with the DNS results.

Figure 4 compares the space-time energy spectra and the temporal spectra at different wave numbers obtained from the DNS and the DAR model with LSE at $y^+ = 5$. The velocities at $y_O^+ = 92$ in the outer layer are used to perform the LSE. Again, the results from the DAR model with LSE are in agreement with those from the DNS. Figure 5 plots the temporal evolutions of the streamwise velocity fluctuations at $y^+ = 5$ obtained from the LSE, the DAR model, and the combination of the DAR model with LSE. The preference angles of the velocity contours obtained from LSE are significantly smaller than those from the DAR, indicating that the large-scale motions propagate more quickly than the small-scale motions near the wall [14]. The DAR result is consistent with the result obtained from the remaining part of the near-wall velocity fluctuations. Consequently, the result obtained from the DAR model with LSE is consistent with the DNS result.
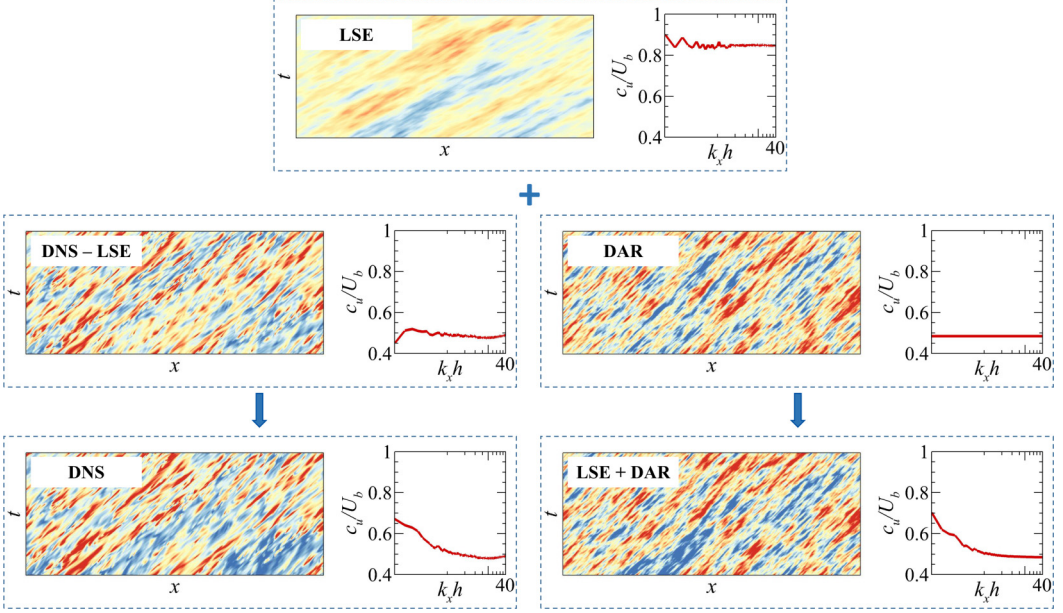
FIG. 5. Temporal evolutions and wave-number-dependent convection velocities of the streamwise velocity fluctuations at $y^+ = 5$ in turbulent channel flows at $\mathrm{Re}_\tau = 550$. Top: The LSE results. Middle left: Subtraction of LSE from DNS. Middle right: The DAR model. Bottom left: The DNS results. Bottom right: The DAR model with LSE.

The DAR model can be rewritten in matrix form for the velocity component and the external forcing, given by

$$\frac{\partial}{\partial t}\begin{bmatrix} \hat{u}(\boldsymbol{\kappa}, t) \\ \hat{\sigma}(\boldsymbol{\kappa}, t) \end{bmatrix} = \begin{bmatrix} L_{NS}(\boldsymbol{\kappa}) & 1 \\ L_{SW}(\boldsymbol{\kappa}) & L_{NL}(\boldsymbol{\kappa}) \end{bmatrix}\begin{bmatrix} \hat{u}(\boldsymbol{\kappa}, t) \\ \hat{\sigma}(\boldsymbol{\kappa}, t) \end{bmatrix} + \begin{bmatrix} 0 \\ L_F(\boldsymbol{\kappa}) \end{bmatrix}\hat{\xi}(\boldsymbol{\kappa}, t), \tag{48}$$

where $L_{NS}(\boldsymbol{\kappa}) = -ik_x U_c$, $L_{SW}(\boldsymbol{\kappa}) = -b(\boldsymbol{\kappa}) = -(k_x^2 V_x^2 + k_z^2 V_z^2)$, and $L_{NL}(\boldsymbol{\kappa}) = -ik_x U_c - 2q(\boldsymbol{\kappa}) = -ik_x U_c - 2\sqrt{k_x^2 V_x^2 + k_z^2 V_z^2}$. Comparing the matrix differential equation (48) with Eq. (26), we find that (i) the velocity component is not explicitly dependent on white-in-time forcing (hence, the DAR model avoids divergent spectral bandwidths) and (ii) the DAR forcing is dependent on the velocity component through the spectral bandwidth. Thus, the DAR model accounts for the random sweeping effect.

In the Appendix, we describe how the DAR model in HIT is derived from the NS equations, where the operator L_{SW} corresponds to the random sweeping effect. The results show that the DAR model in HIT reproduces the same spectral bandwidths as the random sweeping model.

IV. RECONSTRUCTING SPACE-TIME ENERGY SPECTRA FROM AN INCOMPLETE DATA SET

Reconstructing space-time energy spectra from time series of velocity fluctuations at a limited number of measurement points is important in experimental study. In this section, we discuss the LMW model for this purpose. The central idea is as follows: Space-time energy spectra can be approximately estimated from localized wavelike structures. In terms of definition, for a fixed frequency, a space-time energy spectrum is the Fourier transform of the spatial correlation of temporal Fourier modes with respect to space separation. If the temporal Fourier mode can be approximately represented by a local modulated wave with two local wave numbers, the space-time energy spectrum at a fixed wave number is determined by the ensemble average of the local

modulated waves whose wave numbers are equal to the fixed wave number. The local modulated wave can be estimated from the time series of velocity fluctuations at neighboring measurement points.

The LMW model is given by [30]

$$\frac{\Phi^{\text{LMW}}(k_x, \omega)}{\Phi(\omega)} = \frac{\langle a^2(x, \omega)\delta(k_x - k_x^+(x, \omega))\rangle}{2\langle a^2(x, \omega)\rangle} + \frac{\langle a^2(x, \omega)\delta(k_x - k_x^-(x, \omega))\rangle}{2\langle a^2(x, \omega)\rangle}, \tag{49}$$

$$k_x^+(x, \omega) = \partial_x\theta + a^{-1}\partial_x a, \tag{50a}$$

$$k_x^-(x, \omega) = \partial_x\theta - a^{-1}\partial_x a, \tag{50b}$$

where $k_x^+(x, \omega)$ and $k_x^-(x, \omega)$ are the wave numbers of the local modulated wave and determined by the phase and amplitude derivatives of temporal Fourier modes, as shown in Eq. (50). Again, $a(x, \omega)$ and $\theta(x, \omega)$ are the amplitude and phase of the temporal Fourier mode $\hat{u}(x, \omega)$, respectively, as shown in Eq. (10). In practice, the phase and amplitude derivatives are obtained from differences of temporal Fourier modes at neighboring measurement points; the ensemble average is taken for all measurement points at which the local wave numbers are equal to the desired wave numbers.

The derivation of the LMW model is summarized as follows. The space-time energy spectra can be expressed in terms of the spatial correlations of temporal Fourier modes at two different locations,

$$\frac{\Phi(k_x, \omega)}{\Phi(\omega)} = \frac{1}{2\pi} \int \frac{\langle \hat{u}^*(x, \omega)\hat{u}(x + r, \omega)\rangle}{\langle \hat{u}^*(x, \omega)\hat{u}(x, \omega)\rangle} e^{-ik_x r}dr. \tag{51}$$

It is assumed in the LMW model that the temporal Fourier mode at one point is related to another mode at the adjacent point through a local modulated wave, such that

$$\hat{u}^{\text{LMW}}(x + r, \omega) = \hat{u}(x, \omega)\left[\frac{e^{i(a^{-1}\partial_x a \cdot r - \pi/4)}}{\sqrt{2}} + \frac{e^{-i(a^{-1}\partial_x a \cdot r - \pi/4)}}{\sqrt{2}}\right]e^{i\partial_x\theta \cdot r}. \tag{52}$$

As a result, the local modulated wave is a wavelike structure with a single frequency and two distinct wave numbers. In other words, it is the superposition of two distinct waves. Taking the Taylor expansions of the amplitude and phase in Eq. (52) up to first order, we obtain

$$a^{\text{LMW}}(x + r, \omega) \approx a(x, \omega) + \partial_x a \cdot r, \tag{53a}$$

$$\theta^{\text{LMW}}(x + r, \omega) \approx \theta(x, \omega) + \partial_x\theta \cdot r. \tag{53b}$$

The characteristic length scale r in Eq. (53b) is given by $r \ll (1 + U/\sqrt{\langle u^2 \rangle})(\partial_x\theta)^{-1}$ [30], where U is a local mean velocity and $\sqrt{\langle u^2 \rangle}$ is the rms of the local velocity fluctuation. Substitution of Eq. (52) into Eq. (51) leads to the LMW model. Evidently, the spatial variations in the phase and amplitude are taken into account in the LMW model.

The LMW model is a high-order approximation to temporal Fourier modes in terms of the Taylor expansions of their amplitudes and phases; see Eq. (53). This point of view can be used to re-examine Taylor's model and the local wave number (LW) model [28,29]. In Taylor's model, the temporal Fourier mode is assumed to be a traveling wave of constant convection velocity U. As a result, the amplitude derivative is zero, and the phase derivative is independent of the spatial location. Therefore, the Taylor expansions of its amplitude and phase can be expressed as

$$a^{TA}(x + r, \omega) = a(x, \omega), \tag{54a}$$

$$\theta^{TA}(x + r, \omega) = \theta(x, \omega) + \omega r/U. \tag{54b}$$

Substitution of Eq. (54) into Eq. (51) leads to Taylor's model

$$\frac{\Phi^{TA}(k_x, \omega)}{\Phi(\omega)} = \delta(k_x - \omega/U). \tag{55}$$

Again, it is shown that the energy spectrum from Taylor's model is concentrated on the dispersion relation, $k_x = \omega/U$, leading to vanishing spectral bandwidths.

In the LW model, the temporal Fourier mode is assumed to be a local wave. As a result, the amplitude derivative is zero and the phase derivative is dependent on the spatial location. Therefore, the Taylor expansions of its amplitude and phase can be expressed as

$$a^{LW}(x + r, \omega) = a(x, \omega), \qquad (56a)$$

$$\theta^{LW}(x + r, \omega) = \theta(x, \omega) + \partial_x\theta \cdot r. \qquad (56b)$$

Substitution of Eq. (56) into Eq. (51) leads to the LW model

$$\frac{\Phi^{LW}(k_x, \omega)}{\Phi(\omega)} = \frac{\langle a^2(x, \omega)\delta(k_x - k_x^{LW}(x, \omega))\rangle}{\langle a^2(x, \omega)\rangle}, \qquad (57)$$

$$k_x^{LW}(x, \omega) = \partial_x\theta. \qquad (58)$$

The above discussions highlight an attack line to reconstruct space-time energy spectra by successive approximation to energetic coherent structures in turbulent flows.

The LMW model can be shown to exactly reproduce the mean wave number and spectral bandwidth, which are given in Eqs. (11) and (12). The LW model exactly reproduces the mean wave number. However, this model underpredicts spectral bandwidths since the second term in the right-hand side of Eq. (12) is zero. The LMW model is consistent with the dynamics of the turbulent passage. The decorrelation of small-scale structures is affected by the shearing of large-scale eddies and the interaction of smaller-scale eddies, resulting in variations in both phase and amplitude. In the LMW model, the variations are approximately represented by local modulated waves. Note that the LMW model can also be performed for the spatial Fourier mode, in which the local wave number is replaced by the instantaneous frequency.

The LMW model is used for the space-time energy spectra of the streamwise velocity fluctuations in turbulent channel flows at $\mathrm{Re}_\tau = 550$ [30]. The time series of velocity fluctuations $u(x, y, z, t)$ and $u(x + \Delta x, y, z, t)$ at pair points are extracted from the DNS data, with the separation distance Δx taken to be the streamwise grid size Δ_x. To perform the ensemble averages in Eq. (49), spatial locations (x, z) are taken on the x-z plane for every 10 grid points in the streamwise direction and every grid point in the spanwise direction. The total sampling time is $5.12h/U_b$. The Hanning window is applied to the time series to minimize spectral leakage. The spatial averages can be replaced by temporal averages if the total sampling time at a pair of neighboring points is sufficiently large. Figure 6 compares the space-time energy spectra and the spatial spectra at different frequencies obtained from the DNS and the LMW model at $y^+ = 92$. Both the line contours and the spatial spectra at different frequencies from the LMW model are in good agreement with those from the DNS. Furthermore, it was shown [30] that the relative errors of the bandwidths at $y^+ = 92$ from the LMW model are less than 10% for low and moderate frequencies at $\Delta x^+ \approx 90$. Wang *et al.* [72] used the LMW model to reconstruct the space-time energy spectrum from the spatial mode in turbulent channels, where the instantaneous frequency is taken. Their results show that the LMW model ensures correct convection velocities and spectral bandwidths at all scales and represents the most relevant energy in the frequency wave-number domain. In addition, the LMW model can accurately reconstruct the space-time energy spectrum of a propagating Gaussian signal modulated by a nonpropagating Gaussian amplitude [30]. These results show that the LMW model not only provides a method to reconstruct the space-time energy spectra but also offers a theoretical tool to study the coupling of propagation and distortion in turbulent flows.

Finally, we briefly review the application of the LW model to estimate local space-time energy spectra. For spatially evolving flows, such as wakes, jets, and separated flows, velocity fluctuations are inhomogeneous in the streamwise direction. As a result, there is no global wave that is translation invariant. In this case, a local wave number has to be introduced to represent the dependence of Fourier modes on locations. Therefore, a local energy spectrum is defined as the energy density
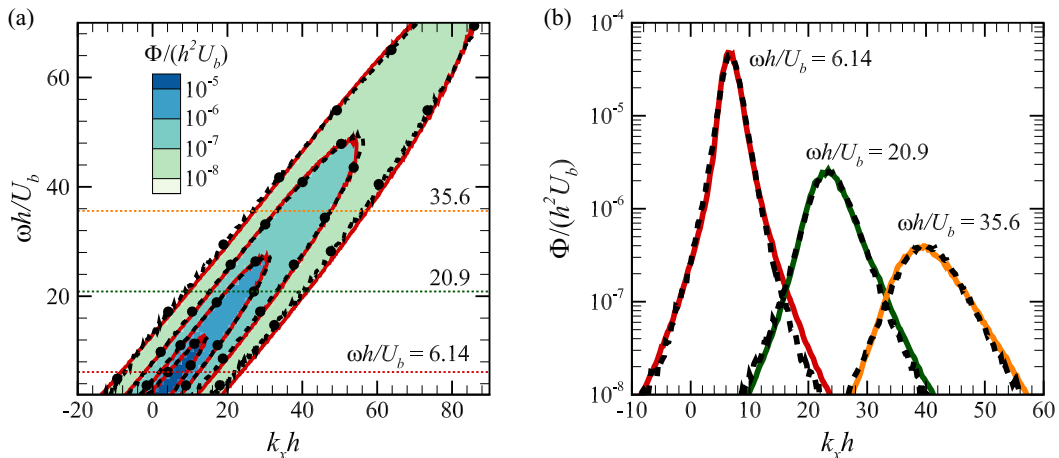
FIG. 6. Comparison of the space-time energy spectra obtained from the DNS and the LMW model for the streamwise velocity fluctuations at $y^+ = 92$ in turbulent channel flows at $\mathrm{Re}_\tau = 550$. (a) Contours obtained from the DNS (colored shades with solid lines) and the LMW model (dashed lines with dots). (b) Cuts through space-time energy spectra at three different frequencies obtained from the DNS (colored solid lines) and the LMW model (dashed lines).

of the Fourier mode with the local wave number at one location. Jones *et al.* [73] used the LW model to reconstruct the local space-time energy spectra of the velocity fluctuations in the plane wake transition. The results show that the spectral bandwidth is very small in the transition region and large in the turbulent region. In addition, throughout the transition, the spectral bandwidth is smaller for the coherent frequencies and larger for those far away from the coherent frequencies. They further demonstrated the significant difference between the local spatial spectra obtained from the LW model and those from Taylor's model in the turbulent region. Thomas and Chu [74] obtained similar observations in the plane jet transition. Mostafa *et al.* [75] used the LW model to study the local space-time energy spectrum of the surface pressure fluctuations in the separation region of the flow around a bluff body. Their measurements show that the local space-time energy spectrum is dominated by large-scale motions in the early region of separation and is distributed over a broad range of frequencies and wave numbers in the region where intermittent reattachment occurs. de Kat and Ganapathisubramani [29] used the LW model to investigate the space-time energy spectra and the spatial energy spectra of velocity fluctuations in a turbulent boundary layer at $\mathrm{Re}_\tau = 2700$. Their results show that the premultiplied spatial spectrum obtained by the LW model exhibits a single peak, while the premultiplied spatial spectrum obtained by Taylor's model displays the double peak.

V. SUMMARY AND FUTURE WORK

The preliminary characterization of space-time energy spectra in turbulent flows is that the energy density distributes over a broad range of wave numbers and frequencies. The two-dimensional surfaces of space-time energy spectra spread to large wave numbers and frequencies and decay most slowly in the direction of convection velocity. Analogous to the probability distribution, space-time energy spectra can be described by using conditional moments. The first-order conditional moments at a fixed frequency (wave number) give mean wave numbers (frequencies), which are used to calculate the scale-dependent convection velocities. The second-order conditional moments at a fixed frequency or wave number give spectral bandwidths, which measure the spreading of energy density distributions. Higher order conditional moments can also be introduced to describe space-time energy spectra.

Taylor's frozen-flow hypothesis and Kraichnan-Tennekes random sweeping hypothesis proposed a picture for turbulent passage. This picture can be used to understand the decorrelation process of turbulent fluctuations and develop the models of space-time energy spectra. The energy cascade process alone, which leads to the scaling of spatial energy spectra, is not sufficient to determine space-time energy spectra. However, it remains a challenge to find an exact expression for space-time energy spectra from the NS equations, analogous to the Kármán-Howarth equation for spatial correlations, to better understand the picture of turbulent passage.

Three distinct approaches of successive approximation have been used to develop the models of space-time energy spectra. The first approach is the successive approximation of the contours of space-time correlations or energy spectra [18,19]: the first-order approximation leads to Taylor's model, and the second-order approximation leads to the EA model. The second approach is the successive approximation of flow patterns in turbulent flows [30]: the first approximation is the local waves that yield the LW model, and the second approximation is the local modulated waves that yield the LMW model. The third approach is the dynamic autoregression of velocity fluctuations [27]: If we start with Taylor's model, the first autoregression results in white-in-time random forcing and the second autoregression results in dynamic autoregressive forcing.

Physics-based or data-driven stochastic dynamic models for space-time energy spectra have been developed to investigate coherent structures [24,49,50,55,56] and enrich large-eddy simulations [76,77]. Taylor's model used in the DAR model can be replaced by LNSEs to study the spatiotemporal dynamics of coherent structures. In fact, LNSEs and the resolvent operator with random forcing are successfully used to study the dynamic evolution of streamwise vortices and streaks in wall-bounded turbulence [39,45,49]. The LNSEs with random forcing are hopefully used to generate turbulent fluctuations that are unresolved in conventional large-eddy simulations, such as missing scales in turbulence-generated noise and turbulent mixing. It remains a challenge to develop the LNSEs with random forcing to reproduce the space-time energy spectra of near-wall velocity fluctuations in wall-modeled large-eddy simulations [27].

APPENDIX: THE DAR MODEL FOR HOMOGENEOUS ISOTROPIC TURBULENCE

In HIT, Kraichnan [12] and Tennekes [13] used the random sweeping hypothesis to describe the distortion caused by the small-scale interaction. The random sweeping model gives the decorrelation timescales and thus predicts the spectral bandwidths. In this Appendix, we show that the DAR model reproduces the same spectral bandwidths as the Kraichnan-Tennekes random sweeping model.

We start with the Fourier representation of the NS equations in HIT [78]

$$\frac{\partial \hat{u}_i(\mathbf{k}, t)}{\partial t} = \hat{\sigma}_i(\mathbf{k}, t) - \nu k^2 \hat{u}_i(\mathbf{k}, t), \tag{A1a}$$

$$\hat{\sigma}_i(\mathbf{k}, t) = -\frac{i}{2} P_{ijm}(\mathbf{k}) \sum_{\mathbf{p}+\mathbf{q}=\mathbf{k}} [\hat{u}_j(\mathbf{p}, t)\hat{u}_m(\mathbf{q}, t)], \tag{A1b}$$

where $\hat{\sigma}_i(\mathbf{k}, t)$ denotes the sum of the nonlinear convection terms and the pressure gradient terms. It is treated as nonlinear forcing in the framework of the resolvent operator. The nonlinear forcing is solenoidal, such as $k_i\hat{\sigma}_i = 0$. $P_{ijm}(\mathbf{k}) = k_m P_{ij}(\mathbf{k}) + k_j P_{im}(\mathbf{k})$ and $P_{ij}(\mathbf{k}) = \delta_{ij} - k_i k_j/k^2$ are the projection tensors. For wave number $\mathbf{k}$ in the inertial range, the viscous term in Eq. (A1a) can be ignored.

The DAR forcing for HIT can be deduced from the NS equations, given by

$$\frac{\partial \hat{\sigma}_i(\mathbf{k}, t)}{\partial t} = -k^2 \mathrm{v}^2 \hat{u}_i(\mathbf{k}, t) - \eta(k)\hat{\sigma}_i(\mathbf{k}, t) + D(k)\hat{\xi}_i(\mathbf{k}, t). \tag{A2}$$

Here, $\eta(k)$ is the damping coefficient. $\hat{\xi}_i(\mathbf{k}, t)$ is a solenoidal and white-in-time random forcing with its intensity $D(k)$. The most important parameter, expressed as $\mathrm{v}^2 = \langle u_1^2 \rangle = \sum_{\mathbf{q}} [\hat{u}_1(-\mathbf{q}, t)\hat{u}_1(\mathbf{q}, t)]$, is the variance of one velocity component. We analytically solve Eqs. (A1a) and (A2) to obtain the velocity modes, which give the spectral bandwidths

$$B(\mathbf{k}) = k^2 \mathrm{v}^2. \tag{A3}$$

This is exactly the same as the results from the Kraichnan-Tennekes random sweeping model.

The main derivation can be described as follows:

(i) Governing equations of nonlinear forcing

Taking the time derivative of $\hat{\sigma}_i(\mathbf{k}, t)$ and using the property of the projection tensors $P_{ijm}(\mathbf{k}) = P_{imj}(\mathbf{k})$, we obtain

$$\frac{\partial \hat{\sigma}_i(\mathbf{k}, t)}{\partial t} = -i P_{ijm}(\mathbf{k}) \sum_{\mathbf{p}+\mathbf{q}=\mathbf{k}} \left[\frac{\partial \hat{u}_j(\mathbf{p}, t)}{\partial t} \hat{u}_m(\mathbf{q}, t) \right]. \tag{A4}$$

Substitution of Eq. (A1) into Eq. (A4) leads to

$$\frac{\partial \hat{\sigma}_i(\mathbf{k}, t)}{\partial t} = T_i(\mathbf{k}, t) + Q_i(\mathbf{k}, t), \tag{A5}$$

where

$$T_i(\mathbf{k}, t) = -\hat{u}_l(\mathbf{k}, t) P_{ijm}(\mathbf{k}) \sum_{\mathbf{q}} [P_{jls}(\mathbf{k} - \mathbf{q})\hat{u}_s(-\mathbf{q}, t)\hat{u}_m(\mathbf{q}, t)], \tag{A6}$$

$$Q_i(\mathbf{k}, t) = -\frac{1}{2} P_{ijm}(\mathbf{k}) \sum_{\substack{\mathbf{k}'+\mathbf{p}'+\mathbf{q}=\mathbf{k} \\ \mathbf{k}'\neq\mathbf{k}, \mathbf{p}'\neq\mathbf{k}, \mathbf{q}\neq\mathbf{k}}} [P_{jls}(\mathbf{k} - \mathbf{q})\hat{u}_l(\mathbf{k}', t)\hat{u}_s(\mathbf{p}', t)\hat{u}_m(\mathbf{q}, t)]$$

$$+ i\nu P_{ijm}(\mathbf{k}) \sum_{\mathbf{p}+\mathbf{q}=\mathbf{k}} [p^2 \hat{u}_j(\mathbf{p}, t)\hat{u}_m(\mathbf{q}, t)]. \tag{A7}$$

Note that the summation in $T_i(\mathbf{k}, t)$ contains the energy factor $\hat{u}_s(-\mathbf{q}, t)\hat{u}_m(\mathbf{q}, t)$. $Q_i(\mathbf{k}, t)$ consists of two parts: the first part is the summation of wave-number triplets $\mathbf{k}'$, $\mathbf{p}'$, and $\mathbf{q}$, in which $\mathbf{k}' \neq \mathbf{k}$, $\mathbf{p}' \neq \mathbf{k}$, and $\mathbf{q} \neq \mathbf{k}$; the second part is the summation of wave-number pairs. $T_i(\mathbf{k}, t)$ and $Q_i(\mathbf{k}, t)$ are evaluated by using LSE. The coherent parts in $T_i(\mathbf{k}, t)$ and $Q_i(\mathbf{k}, t)$ relative to $\hat{u}_i(\mathbf{k}, t)$ are given in (ii) and (iii). The incoherent parts in $T_i(\mathbf{k}, t)$ and $Q_i(\mathbf{k}, t)$ relative to $\hat{u}_i(\mathbf{k}, t)$ are modeled by using damping and white-in-time noise since they are most responsible for energy transfer and random backscattering. It is noted in this case that the intensities of damping and the white-in-time noise do not change the spectral bandwidths.

(ii) LSE of $T_i(\mathbf{k}, t)$

The first part $T_i(\mathbf{k}, t)$ can be simplified by using Kraichnan's approximation in DIA [78]: The energy factor $\hat{u}_s(-\mathbf{q}, t)\hat{u}_m(\mathbf{q}, t)$ with $|\mathbf{q}| \ll |\mathbf{k}|$ is dominant, where the wave number $\mathbf{k}$ is in the inertial range. In this case, the approximation $P_{jls}(\mathbf{k} - \mathbf{q}) \approx P_{jls}(\mathbf{k})$ can also be made. Therefore, we obtain

$$T_i(\mathbf{k}, t) \approx -\hat{u}_l(\mathbf{k}, t) P_{ijm}(\mathbf{k}) P_{jls}(\mathbf{k}) \sum_{\mathbf{q}} [\hat{u}_s(-\mathbf{q}, t)\hat{u}_m(\mathbf{q}, t)]$$

$$= -\hat{u}_l(\mathbf{k}, t)P_{ijm}(\mathbf{k})P_{jls}(\mathbf{k})\mathrm{v}^2\delta_{sm}$$

$$= -\hat{u}_l(\mathbf{k}, t)P_{ijm}(\mathbf{k})P_{jlm}(\mathbf{k})\mathrm{v}^2. \tag{A8}$$

In LSE, the coherent portion in $T_1(\mathbf{k}, t)$ relative to $\hat{u}_1(\mathbf{k}, t)$ is expressed as follows:

$$T_1^{\mathrm{LSE}}(\mathbf{k}, t) = \alpha(\mathbf{k})\hat{u}_1(\mathbf{k}, t), \tag{A9}$$

where

$$\alpha(\mathbf{k}) = \frac{\langle \hat{u}_1^*(\mathbf{k}, t)T_1(\mathbf{k}, t)\rangle}{\langle \hat{u}_1^*(\mathbf{k}, t)\hat{u}_1(\mathbf{k}, t)\rangle}. \tag{A10}$$

The following relationship exists for the velocity spectrum tensor in HIT [79]:

$$\frac{\langle \hat{u}_1^*(\mathbf{k}, t)\hat{u}_i(\mathbf{k}, t)\rangle}{\langle \hat{u}_1^*(\mathbf{k}, t)\hat{u}_1(\mathbf{k}, t)\rangle} = \frac{P_{1i}(\mathbf{k})}{P_{11}(\mathbf{k})}. \tag{A11}$$

Substituting Eq. (A11) into Eq. (A10), we obtain

$$\alpha(\mathbf{k}) = -k^2\mathrm{v}^2. \tag{A12}$$

Therefore, we have

$$T_i^{\mathrm{LSE}}(\mathbf{k}, t) = -k^2\mathrm{v}^2\hat{u}_i(\mathbf{k}, t). \tag{A13}$$

Note that $\alpha(\mathbf{k})$ depends on the magnitude of the wave-number vector $\mathbf{k}$ but is independent of its direction.

(iii) LSE of $Q_i(\mathbf{k}, t)$

In LSE, the coherent portion in $Q_1(\mathbf{k}, t)$ relative to $\hat{u}_1(\mathbf{k}, t)$ is expressed as follows:

$$Q_1^{\mathrm{LSE}}(\mathbf{k}, t) = \beta(\mathbf{k})\hat{u}_1(\mathbf{k}, t), \tag{A14}$$

where

$$\beta(\mathbf{k}) = \frac{\langle \hat{u}_1^*(\mathbf{k}, t)Q_1(\mathbf{k}, t)\rangle}{\langle \hat{u}_1^*(\mathbf{k}, t)\hat{u}_1(\mathbf{k}, t)\rangle}. \tag{A15}$$

There are two parts in $Q_1(\mathbf{k}, t)$: $\hat{u}_l(\mathbf{k}', t)\hat{u}_s(\mathbf{p}', t)\hat{u}_m(\mathbf{q}, t)$ ($\mathbf{k}' \neq \mathbf{k}$, $\mathbf{p}' \neq \mathbf{k}$, $\mathbf{q} \neq \mathbf{k}$) and $\hat{u}_j(\mathbf{p}, t)\hat{u}_m(\mathbf{q}, t)$. According to the normality hypothesis, the correlations of the two parts with $\hat{u}_1^*(\mathbf{k}, t)$ are zero, that is to say,

$$\beta(\mathbf{k}) = 0. \tag{A16}$$

Therefore, $Q_i(\mathbf{k}, t)$ does not contain any coherent portion relative to $\hat{u}_i(\mathbf{k}, t)$.

---

[1] G. W. He, G. D. Jin, and Y. Yang, Space-time correlations and dynamic coupling in turbulent flows, Annu. Rev. Fluid Mech. **49**, 51 (2017).

[2] R. H. Kraichnan, Isotropic turbulence and inertial-range structure, Phys. Fluids **9**, 1728 (1966).

[3] J. LeHew, M. Guala, and B. J. McKeon, A study of the three-dimensional spectral energy distribution in a zero pressure gradient turbulent boundary layer, Exp. Fluids **51**, 997 (2011).

[4] P. C. di Leoni, P. J. Cobelli, and P. D. Mininni, The spatio-temporal spectrum of turbulent flows, Eur. Phys. J. E. **38**, 136 (2015).

[5] W. R. Graham, A comparison of models for the wavenumber-frequency spectrum of turbulent boundary layer pressures, J. Sound Vib. **206**, 541 (1997).

[6] G. W. He, M. Wang, and S. K. Lele, On the computation of space-time correlations by large-eddy simulation, Phys. Fluids **16**, 3859 (2004).

[7] M. Slama, C. Leblond, and P. Sagaut, A Kriging-based elliptic extended anisotropic model for the turbulent boundary layer wall pressure spectrum, J. Fluid Mech. **840**, 25 (2018).

[8] M. Mancinelli, T. Pagliaroli, R. Camussi, and T. Castelain, On the hydrodynamic and acoustic nature of pressure proper orthogonal decomposition modes in the near field of a compressible jet, J. Fluid Mech. **836**, 998 (2018).

[9] G. I. Taylor, The spectrum of turbulence, Proc. R. Soc. London A **164**, 476 (1938).

[10] C. C. Lin, On Taylor's hypothesis and the acceleration terms in the Navier-Stokes equations, Q. Appl. Math. **10**, 295 (1953).

[11] J. L. Lumley, Interpretation of time spectra measured in high-intensity shear flows, Phys. Fluids **8**, 1056 (1965).

[12] R. H. Kraichnan, Kolmogorov's hypotheses and Eulerian turbulence theory, Phys. Fluids **7**, 1723 (1964).

[13] H. Tennekes, Eulerian and Lagrangian time microscales in isotropic turbulence, J. Fluid Mech. **67**, 561 (1975).

[14] J. C. Del Álamo and J. Jiménez, Estimation of turbulent convection velocities and corrections to Taylor's approximation, J. Fluid Mech. **640**, 5 (2009).

[15] M. Wilczek and Y. Narita, Wave-number-frequency spectrum for turbulence from a random sweeping hypothesis with mean flow, Phys. Rev. E **86**, 066308 (2012).

[16] M. Wilczek, R. J. A. M. Stevens, and C. Meneveau, Spatio-temporal spectra in the logarithmic layer of wall turbulence: Large-eddy simulations and simple models, J. Fluid Mech. **769**, R1 (2015).

[17] L. J. Lukassen, R. J. A. M. Stevens, C. Meneveau, and M. Wilczek, Modeling space-time correlations of velocity fluctuations in wind farms, Wind Energy **21**, 474 (2018).

[18] G. W. He and J. B. Zhang, Elliptic model for space-time correlations in turbulent shear flows, Phys. Rev. E **73**, 055303(R) (2006).

[19] X. Zhao and G. W. He, Space-time correlations of fluctuating velocities in turbulent shear flows, Phys. Rev. E **79**, 046316 (2009).

[20] L. N. Trefethen, A. E. Trefethen, S. C. Reddy, and T. A. Driscoll, Hydrodynamic stability without eigenvalues, Science **261**, 578 (1993).

[21] B. J. McKeon and A. S. Sharma, A critical-layer framework for turbulent pipe flow, J. Fluid Mech. **658**, 336 (2010).

[22] B. J. McKeon, The engine behind (wall) turbulence: Perspectives on scale interactions, J. Fluid Mech. **817**, P1 (2017).

[23] A. Zare, T. T. Georgiou, and M. R. Jovanović, Stochastic dynamical modeling of turbulent flows, Annu. Rev. Control Robot. Auton. Syst. **3**, 195 (2020).

[24] M. R. Jovanović, From bypass transition to flow control and data-driven turbulence modeling: An input-output viewpoint, Annu. Rev. Fluid Mech. **53**, 311 (2021).

[25] C. Liu and D. F. Gayme, An input-output based analysis of convective velocity in turbulent channels, J. Fluid Mech. **888**, A32 (2020).

[26] B. F. Farrell and P. J. Ioannou, Stochastic forcing of the linearized Navier-Stokes equations, Phys. Fluids A **5**, 2600 (1993).

[27] T. Wu and G. W. He, Stochastic dynamical model for space-time energy spectra in turbulent shear flows, Phys. Rev. Fluids **6**, 054602 (2021).

[28] J. M. Beall, Y. C. Kim, and E. J. Powers, Estimation of wavenumber and frequency spectra using fixed probe pairs, J. Appl. Phys. **53**, 3933 (1982).

[29] R. de Kat and B. Ganapathisubramani, Frequency-wavenumber mapping in turbulent shear flows, J. Fluid Mech. **783**, 166 (2015).

[30] T. Wu and G. W. He, Local modulated wave model for the reconstruction of space-time energy spectra in turbulent flows, J. Fluid Mech. **886**, A11 (2020).

[31] A. E. Perry, S. Henbest, and M. S. Chong, A theoretical and experimental study of wall turbulence, J. Fluid Mech. **165**, 163 (1986).

[32] T. B. Nickels, I. Marusic, S. Hafez, and M. S. Chong, Evidence of the k_1^{-1} Law in a High-Reynolds-Number Turbulent Boundary Layer, Phys. Rev. Lett. **95**, 074501 (2005).

[33] D. Chandran, R. Baidya, J. P. Monty, and I. Marusic, Two-dimensional energy spectra in high-Reynolds-number turbulent boundary layers, J. Fluid Mech. **826**, R1 (2017).

[34] H. Mouri, Two-point correlation in wall turbulence according to the attached-eddy hypothesis, J. Fluid Mech. **821**, 343 (2017).

[35] H. Mouri, T. Morinaga, and S. Haginoya, Unlikely existence of k_x^{-1} spectral law in wall turbulence: An observation of the atmospheric surface layer, Phys. Fluids **31**, 035103 (2019).

[36] Y. Narita, Spectral moments for the analysis of frequency shift, broadening, and wave vector anisotropy in a turbulent flow, Earth Planets Space **69**, 73 (2017).

[37] T. Wu, C. H. Geng, Y. C. Yao, C. X. Xu, and G. W. He, Characteristics of space-time energy spectra in turbulent channel flows, Phys. Rev. Fluids **2**, 084609 (2017).

[38] J. M. Wallace, Quadrant analysis in turbulence research: History and evolution, Annu. Rev. Fluid Mech. **48**, 131 (2016).

[39] M. R. Jovanović and B. Bamieh, Componentwise energy amplification in channel flows, J. Fluid Mech. **534**, 145 (2005).

[40] O. Semeraro, V. Jaunet, P. Jordan, A. V. G. Cavalieri, and L. Lesshafft, Stochastic and Harmonic Optimal Forcing in Subsonic Jets, in *22nd AIAA/CEAS Aeroacoustics Conference* (AIAA, Reston, VA, 2016), p. 2935.

[41] A. Towne, O. T. Schmidt, and T. Colonius, Spectral proper orthogonal decomposition and its relationship to dynamic mode decomposition and resolvent analysis, J. Fluid Mech. **847**, 821 (2018).

[42] O. T. Schmidt, A. Towne, G. Rigas, T. Colonius, and G. A. Brès, Spectral analysis of jet turbulence, J. Fluid Mech. **855**, 953 (2018).

[43] L. Lesshafft, O. Semeraro, V. Jaunet, A. V. G. Cavalieri, and P. Jordan, Resolvent-based modeling of coherent wave packets in a turbulent jet, Phys. Rev. Fluids **4**, 063901 (2019).

[44] B. F. Farrell and P. J. Ioannou, Perturbation structure and spectra in turbulent channel flow, Theor. Comput. Fluid Dyn. **11**, 237 (1998).

[45] B. Bamieh and M. Dahleh, Energy amplification in channel flows with stochastic excitation, Phys. Fluids **13**, 3258 (2001).

[46] J. Kim and F. Hussain, Propagation velocity of perturbations in turbulent channel flow, Phys. Fluids A **5**, 695 (1993).

[47] C. H. Geng, G. W. He, Y. S. Wang, C. X. Xu, A. Lozano-Durán, and J. M. Wallace, Taylor's hypothesis in turbulent channel flow considered using a transport equation analysis, Phys. Fluids **27**, 025111 (2015).

[48] A. Towne, G. A. Brès, and S. K. Lele, A statistical Jet-Noise Model Based on the Resolvent Framework, in *23rd AIAA/CEAS Aeroacoustics Conference* (AIAA, Reston, VA, 2017), p. 3706.

[49] P. A. S. Nogueira, P. Morra, E. Martini, A. V. G. Cavalieri, and D. S. Henningson, Forcing statistics in resolvent analysis: Application in minimal turbulent Couette flow, J. Fluid Mech. **908**, A32 (2021).

[50] P. Morra, P. A. S. Nogueira, A. V. G. Cavalieri, and D. S. Henningson, The colour of forcing statistics in resolvent analyses of turbulent channel flows, J. Fluid Mech. **907**, A24 (2021).

[51] K. Rosenberg, S. Symon, and B. J. McKeon, Role of parasitic modes in nonlinear closure via the resolvent feedback loop, Phys. Rev. Fluids **4**, 052601(R) (2019).

[52] B. J. McKeon, A. S. Sharma, and I. Jacobi, Experimental manipulation of wall turbulence: A systems approach, Phys. Fluids **25**, 031301 (2013).

[53] R. Moarref, M. R. Jovanović, J. A. Tropp, A. S. Sharma, and B. J. McKeon, A low-order decomposition of turbulent channel flow via resolvent analysis and convex optimization, Phys. Fluids **26**, 051701 (2014).

[54] R. M. McMullen, K. Rosenberg, and B. J. McKeon, Interaction of forced Orr-Sommerfeld and Squire modes in a low-order representation of turbulent channel flow, Phys. Rev. Fluids **5**, 084607 (2020).

[55] A. Zare, M. R. Jovanović, and T. T. Georgiou, Colour of turbulence, J. Fluid Mech. **812**, 636 (2017).

[56] P. Morra, O. Semeraro, D. S. Henningson, and C. Cossu, On the relevance of Reynolds stresses in resolvent analyses of turbulent wall-bounded flows, J. Fluid Mech. **867**, 969 (2019).

[57] J. C. Del Álamo and J. Jiménez, Linear energy amplification in turbulent channels, J. Fluid Mech. **559**, 205 (2006).

[58] C. Cossu, G. Pujals, and S. Depardon, Optimal transient growth and very large-scale structures in turbulent boundary layers, J. Fluid Mech. **619**, 79 (2009).

[59] G. Pujals, M. García-Villalba, C. Cossu, and S. Depardon, A note on optimal transient growth in turbulent channel flows, Phys. Fluids **21**, 015109 (2009).

[60] Y. Hwang and C. Cossu, Amplification of coherent streaks in the turbulent Couette flow: An input-output analysis at low Reynolds number, J. Fluid Mech. **643**, 333 (2010).

[61] Y. Hwang and C. Cossu, Linear non-normal energy amplification of harmonic and stochastic forcing in the turbulent channel flow, J. Fluid Mech. **664**, 51 (2010).

[62] R. Moarref and M. R. Jovanović, Model-based design of transverse wall oscillations for turbulent drag reduction, J. Fluid Mech. **707**, 205 (2012).

[63] S. J. Illingworth, J. P. Monty, and I. Marusic, Estimating large-scale structures in wall turbulence using linear models, J. Fluid Mech. **842**, 146 (2018).

[64] S. Symon, S. J. Illingworth, and I. Marusic, Energy transfer in turbulent channel flows and implications for resolvent modelling, J. Fluid Mech. **911**, A3 (2021).

[65] E. Pickering, G. Rigas, O. T. Schmidt, D. Sipp, and T. Colonius, Optimal eddy viscosity for resolvent-based models of coherent structures in turbulent jets, J. Fluid Mech. **917**, A29 (2021).

[66] R. D. Cess, A survey of the literature on heat transfer in turbulent tube flow, Res. Rep., 8–0529–R24 (Westinghouse, Pittsburgh, PA, 1958).

[67] W. C. Reynolds and A. K. M. F. Hussain, The mechanics of an organized wave in turbulent shear flow. Part 3. Theoretical models and comparisons with experiments, J. Fluid Mech. **54**, 263 (1972).

[68] A. Towne, A. Lozano-Durán, and X. Yang, Resolvent-based estimation of space–time flow statistics, J. Fluid Mech. **883**, A17 (2020).

[69] E. Martini, A. V. G. Cavalieri, P. Jordan, A. Towne, and L. Lesshafft, Resolvent-based optimal estimation of transitional and turbulent flows, J. Fluid Mech. **900**, A2 (2020).

[70] B. W. Yang, G. D. Jin, T. Wu, Z. X. Yang, and G. W. He, Numerical implementation and evaluation of resolvent-based estimation for space-time energy spectra in turbulent channel flows, Acta Mech. Sin. **36**, 775 (2020).

[71] W. J. Baars, N. Hutchins, and I. Marusic, Spectral stochastic estimation of high-Reynolds-number wall-bounded turbulence for a refined inner-outer interaction model, Phys. Rev. Fluids **1**, 054406 (2016).

[72] H. N. Wang, W. X. Huang, and C. X. Xu, Space-time characteristics of turbulence in minimal flow units, Phys. Fluids **32**, 125103 (2020).

[73] F. L. Jones, C. P. Ritz, R. W. Miksad, E. J. Powers, and R. S. Solis, Measurement of the local wavenumber and frequency spectrum in a plane wake, Exp. Fluids **6**, 365 (1988).

[74] F. O. Thomas and H. C. Chu, Experiments on the nonlinear stages of excited and natural planar jet shear layer transition, Exp. Fluids **14**, 451 (1993).

[75] N. H. Mostafa, M. R. Hajj, M. D. Zeiger, and S. A. Ragab, Space/time characteristics of pressure fluctuations in separation regions, J. Wind Eng. Ind. Aerod. **90**, 415 (2002).

[76] A. S. Ghate and S. K. Lele, Subfilter-scale enrichment of planetary boundary layer large eddy simulation using discrete Fourier-Gabor modes, J. Fluid Mech. **819**, 494 (2017).

[77] A. S. Ghate and S. K. Lele, Gabor mode enrichment in large eddy simulations of turbulent flow, J. Fluid Mech. **903**, A13 (2020).

[78] R. H. Kraichnan, The structure of isotropic turbulence at very high Reynolds numbers, J. Fluid Mech. **5**, 497 (1959).

[79] P. A. Durbin and B. A. P. Reif, *Statistical Theory and Modeling for Turbulent Flows* (John Wiley and Sons, New York, 2011).